THE JOURNAL OF PHYSICAL CHEMISTRY C

pubs.acs.org/JPCC Article

Role of Defects in Photocatalytic Water Splitting: Monodoped vs Codoped $SrTiO_3$

Manish Kumar,* Pooja Basera, Shikha Saini, and Saswata Bhattacharya*

Cite This: J. Phys. Chem. C 2020, 124, 10272−10279 Read Online

ACCESS | Metrics & More | Article Recommendations | Supporting Information

ABSTRACT: Using the hybrid density functional theory and *ab initio* atomistic thermodynamics, we report that monodoping of nonmetal (N) or metal (Mn) in $SrTiO_3$ can induce visible-light absorption, but none of them are suitable to ameliorate the photocatalytic activity. Therefore, in order to achieve enhanced photocatalytic activity of $SrTiO_3$, we have employed codoped Mn and N simultaneously in $SrTiO_3$ to modulate its electronic properties effectively. In the codoped $SrTiO_3$, the recombination of photogenerated charge carriers is suppressed, and the diffusion and mobility are increased owing to the passivation of discrete localized states. Our results reveal that $Mn_{Sr}N_O$ (codoping of Mn at the Sr site and N at the O site) is the most promising candidate for enhancing the photocatalytic activity of $SrTiO_3$ under visible light.

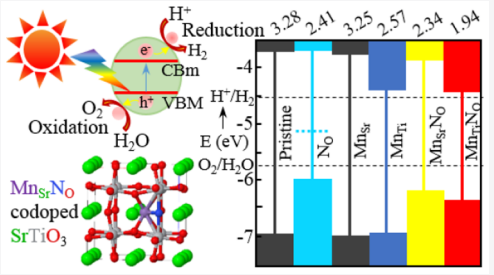

INTRODUCTION

$SrTiO_3$ has emerged as one of the most promising energy materials[1−7] for photocatalytic water splitting.[8−14] However, owing to its large band gap (3.25 eV),[15] its application at a commercial level is delimited. Thus, several works have been endeavored to reduce the band gap of $SrTiO_3$ in order to induce visible-light absorption via doping with metals,[16−20] nonmetals,[21−26] or a combination of several elements.[27−31] However, the band gap reduction cannot ensure the enhancement in photocatalytic efficiency as it also depends on the location of the conduction band minimum (CBm) and valence band maximum (VBM).[32] For transition metal (TM) doped $SrTiO_3$, TM d-states hybridize with those states of the $SrTiO_3$ that contribute to the conduction band, and thus, the reduction in band gap occurs by shifting of CBm in a downward direction. However, due to this, the reducing power is deteriorated. Also, in general, doping by 3d elements leads to localized states in the gap, which are detrimental to the photocatalysis. Therefore, the transition metal alone is not suitable for improvement in photocatalytic activity. On the other hand, nonmetal doped $SrTiO_3$ is found to narrow the band gap by elevating the VBM. However, in this case also, localized states appeared deep inside the forbidden region, which can trap the photoexcited charge carriers and accelerate the electron−hole recombination. This in turn degrades the photocatalytic efficiency.[17,33] This has motivated us for codoping. The codoping with a metal is one of the preeminent solutions to passivate such discrete states of dopants in the forbidden region and form the continuum band.[32−35] Also, earlier studies have suggested that codoping of metal in nonmetal-doped $SrTiO_3$ or TiO_2 stabilizes the system; i.e., the solubility of nonmetal gets increased.[33,36,37] By means of codoping, band edges can be engineered to comply with the needs; i.e., the spectral response expands to the visible region while retaining the reduction and oxidation power.[38,39] A thorough screening of the codopants has been done by calculating the band gap (see Table S1 in Supporting Information (SI)). From here, we have identified few promising systems (marked as red), and one of them is the N and Mn codoped system. The decrement in band gap is most suitable for the Mn and N codoped system, whereas in the rest of the cases, the band gap decrement is either larger or smaller than what is needed for the maximum efficiency in photocatalytic water splitting (∼2 eV[40,41]). Moreover, one of the important factors for choosing Mn is that it has a d−d transition, and its d-orbital's energy facilitates the suitable potentials for water redox reactions. Note that the individual monodopants (i.e., N and Mn) have already been experimentally synthesized.[24,42−45] However, for the codoping of Mn and N in bulk $SrTiO_3$, any experimental or theoretical reports are hitherto unknown.

In this article, we have, therefore, studied codoped (N−Mn) $SrTiO_3$ for enhancing the photocatalytic efficiency under visible light. To understand the N−Mn codoped case, first we have addressed the respective monodoped (N, Mn) cases and their thermodynamic stability using hybrid density functional theory (DFT)[46,47] and *ab initio* atomistic thermodynamics at realistic conditions (temperature (T), partial pressure of

Received: November 30, 2019
Revised: April 1, 2020
Published: April 7, 2020

https://dx.doi.org/10.1021/acs.jpcc.9b11160
J. Phys. Chem. C 2020, 124, 10272−10279

oxygen (p_{O_2}), and doping).[48] Next, to get the insights on the synergistic effect of codoping, electronic density of states for pristine, monodoped, and codoped $SrTiO_3$ have been compared. In addition, the optical response using the single-shot G_0W_0[49,50] method is also analyzed. Finally, from the perspective of its usage in photocatalytic water splitting, we have examined the band-edge alignment of (un)doped $SrTiO_3$ w.r.t. water redox potential levels.

COMPUTATIONAL METHODS

We have carried out the DFT calculations using the Vienna *ab initio* simulation package (VASP).[51,52] The projector-augmented wave (PAW) potentials[53] are used to describe the ion−electron interactions in all the elemental constituents, viz., Sr, Ti, Mn, O, and N, that contain ten, four, seven, six, and five valence electrons, respectively. The total energy calculations are performed using the hybrid exchange−correlation (xc) functional HSE06[54] (for validation of xc functionals, see Section VI in the SI). To introduce defects in $SrTiO_3$, we have used a 40-atom supercell, which is constructed by a 2 × 2 × 2 repetition of cubic $SrTiO_3$ unit cell (5 atoms). A k-point mesh of 4 × 4 × 4 is used, which is generated using a Monkhorst−Pack[55] scheme. The self-consistency loop is converged with a threshold of 0.01 meV energy. The cutoff energy of 600 eV is used for the plane-wave basis set. Note that we have performed the spin-polarized calculations because the doped systems contain unpaired electrons. The quasiparticle energy calculations have been carried out using a single-shot G_0W_0 approximation starting from the orbitals obtained using the HSE06 xc functional. The polarizability calculations are performed on a grid of 50 frequency points. To make computation feasible, the number of bands is set to 384, which is typically four times the number of occupied orbitals.

RESULTS AND DISCUSSION

Stability of Defects in $SrTiO_3$: *Ab Initio* Atomistic Thermodynamics. On doping $SrTiO_3$ with a nonmetal dopant (e.g., N), the possible defects that could occur are N_O (N substituted at the O position), N_i (N as an interstitial making a bond with O), and $(N_2)_O$ split-interstitial (one N is at the interstitial position, and another one is substituted by the nearby O, making a bond with each other).[24,42,43,56] In the case of metal (e.g., Mn) doping, Mn could be substituted at either the Ti (Mn_{Ti}) or Sr (Mn_{Sr}) site, or it could also be present as an interstitial (Mn_i) in $SrTiO_3$.[44,45] Note that these defects are not stable in neutral form because of the uncompensated charge. Therefore, we have calculated the stability of charged defects in addition to neutral defects with charge states q (−2, −1, 0, +1, +2).[48,56,57]

To analyze the thermodynamic stability of the defected configuration w.r.t. pristine $SrTiO_3$, we have calculated the formation energy by means of *ab initio* atomistic thermodynamics.[48,57−60] For an X-related defect with charge state q, the formation energy ($E_f(X^q)$) is calculated as follows[48,56,57]

$$E_f(X^q) = E_{tot}(X^q) - E_{tot}(\text{pristine}^0) - \sum_i n_i\mu_i + q(\mu_e + \text{VBM} + \Delta V) \quad (1)$$

where $E_{tot}(X^q)$ and $E_{tot}(\text{pristine}^0)$ are the total DFT energies with defect (at charge q) and pristine neutral, respectively. n_i is the number of atoms i added (positive) or removed (negative) from the system, and μ_i is the corresponding chemical potential. μ_i is referenced from the total DFT energy ($E_{tot}(i)$) of species i, i.e., $\mu_i = \Delta\mu_i + E_{tot}(i)$. The chemical potentials, $\Delta\mu_i$, have been chosen carefully to reflect the appropriate environmental growth conditions (see section II in SI). μ_e is the chemical potential of the electron varied from the VBM to CBm of the pristine system, and ΔV accounts for the core level alignment of the defected system w.r.t. the pristine neutral system.

The optimized structures of all the doped and pristine $SrTiO_3$ supercells are shown in Figure S1. $SrTiO_3$ has a cubic structure space group $Pm\bar{3}m$ at room temperature. On doping N in pristine, N-related defects, viz., N_O, N_i, and $(N_2)_O$, could form. N_O shows negligible distortion, whereas N_i and $(N_2)_O$ show more distortion in the lattice. We can sum up about the stability of all three configurations of N-related defects at different environmental conditions by observing the 3D phase diagram as shown in Figure 1a. Here, on the x-axis, $\Delta\mu_O$ is varied from O-poor to O-rich conditions in accordance with T and p_{O_2}. On the y-axis, we have scanned the entire forbidden region by means of μ_e, which is referenced from the VBM of pristine $SrTiO_3$. On the z-axis, we have shown the most stable phases having a minimum formation energy at a given environmental condition using the colored surfaces. The charge states +1 and −1 are energetically stable in the case of N_O near the VBM and CBm, respectively. N_i is energetically stable in charge states +1, 0, and −1. The positive charge states

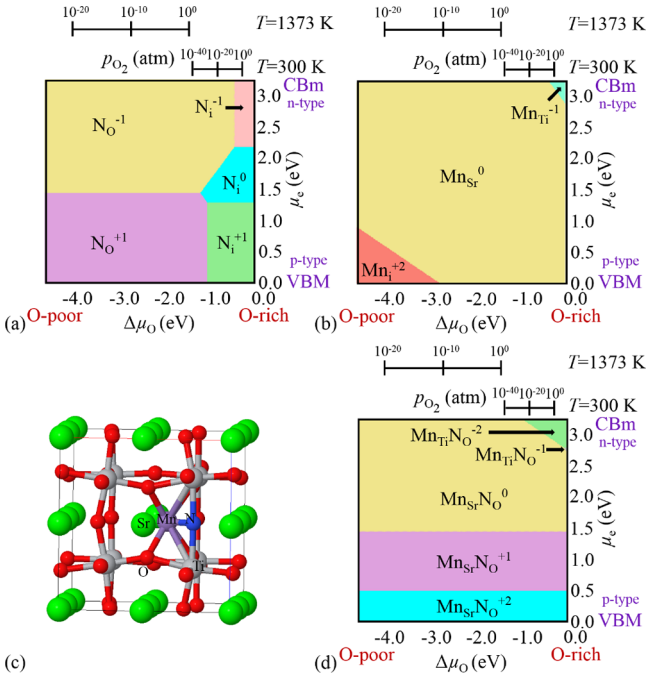

Figure 1. 2D projection of the 3D phase diagram that manifests the stable phases of (a) N-related, (b) Mn-related, and (d) (N−Mn)-related charged defects having minimum formation energy as a function of μ_e and $\Delta\mu_O$. Here, on the x-axis, $\Delta\mu_O$ is varied according to T and p_{O_2}, and on the y-axis, μ_e is varied from the VBM to CBm of the pristine $SrTiO_3$. Colored regions show the most stable phases having a minimum formation energy at a given environmental condition. Top axes are showing the pressure (p_{O_2}) range at two temperatures: T = 300 and 1373 K. (c) Ball and stick model of the optimized structure of $Mn_{Sr}N_O$ defect configuration.

https://dx.doi.org/10.1021/acs.jpcc.9b11160
J. Phys. Chem. C 2020, 124, 10272−10279

are more favorable for smaller values of μ_e, i.e., near the VBM (p-type), whereas negative charge states are stable near the CBm (n-type) for a larger value of μ_e. Since O-poor and O-rich conditions also correspond to lesser and more content of O, respectively; therefore, N_O is more difficult/easier to form in O-rich/O-poor conditions. N_O is stable with the charge state −1 near CBm, as it has one electron less than the O atom. The thermodynamic transition level (±) lies in between the VBM and CBm, indicating that N_O acts as both a deep donor/acceptor depending on the nature of doping (i.e., p-type or n-type). From Figure 1a, we can easily see that N_O is the predominant defect in N-doped $SrTiO_3$ for a wide range of environmental conditions including the experimental growth condition (T = 1373 K, p_{O_2} = 1 atm[23]), whereas N_i is only favorable in O-rich conditions (in accordance with the 2D phase diagram (see Figure S2)).

On doping Mn in $SrTiO_3$, the structures that could form are Mn_{Sr}, Mn_{Ti}, and Mn_i. In the case of Mn_{Sr}, only a neutral defect is stable, which signifies that Mn exists in the Mn^{2+} oxidation state when substituted at the Sr (Sr^{2+} oxidation state) site in $SrTiO_3$ (see Figure 1b). Mn_{Ti} is stable in the −1 charge state, indicating that in addition to the Mn^{4+} oxidation state the Mn^{3+} oxidation state could also exist, though unlikely, when Mn is substituted at the Ti (Ti^{4+} oxidation state) site. Mn_i with +2 charge state is stable in p-type $SrTiO_3$ under O-poor conditions, while Mn_{Ti} with a −1 charge state is stable in n-type $SrTiO_3$ under O-rich conditions, as shown in the 3D phase diagram (see Figure 1b). Neutral Mn_{Sr} is the prominent defect under all the three environmental conditions. The formation energy for Mn-doped $SrTiO_3$ in all oxygen environmental conditions is small, particularly in O-intermediate conditions (see Figure S3), which implies that it is easier to dope Mn in $SrTiO_3$.

From the above analysis, we conclude that in the case of monodoped $SrTiO_3$ substitutional doping is the most stable for a wider region of the environmental conditions, including the experimental growth conditions. Therefore, we have considered only the substitutional position for codoping of Mn and N in $SrTiO_3$. The formation energy of $Mn_{Sr}N_O$ ($E_f(Mn_{Sr}N_O^q)$) is calculated as follows

$$E_f(Mn_{Sr}N_O^q) = E_{tot}(Mn_{Sr}N_O^q) - E_{tot}(SrTiO_3^0) + \mu_O - \mu_N + \mu_{Sr} - \mu_{Mn} + q(\mu_e + VBM + \Delta V) \quad (2)$$

where $E_{tot}(Mn_{Sr}N_O^q)$ and $E_{tot}(SrTiO_3^0)$ are the DFT energies of the codoped system (Mn at Sr and N at O) with charge q and the pristine neutral $SrTiO_3$, respectively. μ_O and μ_N are the chemical potentials of the oxygen and nitrogen atom, referenced from the total DFT energy with the addition of zero-point energy of O_2 and N_2 molecules, respectively, i.e., $\mu_O = \Delta\mu_O + \frac{1}{2}\left(E_{tot}(O_2) + \frac{h\nu_{OO}}{2}\right)$ and $\mu_N = \Delta\mu_N + \frac{1}{2}\left(E_{tot}(N_2) + \frac{h\nu_{NN}}{2}\right)$. In the latter terms, ν_{OO} and ν_{NN} are the O−O and N−N stretching frequencies, respectively. The chemical potential $\mu_X = \Delta\mu_X + E_{tot}(X)$ (where X = Mn, Sr, and Ti). The chemical potential $\Delta\mu_X$ (X = O, N, Mn, Sr, and Ti) is chosen carefully (see Section II in the SI). Figure 1d shows the 3D phase diagram for the stability of codoped systems. $Mn_{Sr}N_O$ is the predominant defect in all the environmental growth conditions and is stable in +2, +1, and neutral charge states [the results are in accordance with the 2D phase diagram (see Figure S4)]. This will act as a donor in p-type $SrTiO_3$, whereas $Mn_{Ti}N_O$ is stable only for a smaller region in extreme O-rich/Ti-poor condition with charge states −1 and −2 near CBm (n-type); i.e., it will act as an acceptor (see Figure 1d). To further confirm that the formation of the defect pair (N−Mn) in $SrTiO_3$ is stable, the binding energy (E_b) of the defect pairs (N−Mn) in $SrTiO_3$ has also been checked.[32,61] (We have taken the difference between total DFT energies (of codoped and pristine $SrTiO_3$) and total DFT energies (of respective monodoped $SrTiO_3$), which is opposite to what has been considered in refs 32 and 61. Therefore, the pair that has negative binding energy is stable.) A more negative value of E_b indicates that the defect pair is more stable when both the dopants are present in the sample. E_b values for $Mn_{Sr}N_O$ and $Mn_{Ti}N_O$ pairs are −1.46 and −0.33 eV, respectively. These values indicate that defect pairs are more stable than the isolated impurities in the $SrTiO_3$ supercell. Also, $Mn_{Sr}N_O$ is a more stable configuration than $Mn_{Ti}N_O$ since $Mn_{Sr}N_O$ has higher (more negative) binding energy than $Mn_{Ti}N_O$. In the codoped system, Mn acts as a donor, whereas N acts as an acceptor. The charge transfer takes place from the donor to acceptor, and strong Coulomb interaction arises between a positively charged donor and negatively charged acceptor. Hence, the defect pair is stable. The extra stability in $Mn_{Sr}N_O$ is due to the shift of Mn away from the Sr center toward N as shown in Figure 1c and making strong bonds with its neighbor atoms.

Electronic Structure Analysis. To get more insights about the effect of dopants in $SrTiO_3$, we have calculated atom projected density of states (pDOS). The DOS plots for pristine and monodoped $SrTiO_3$ are shown in Figure 2(a−d). In pristine $SrTiO_3$, the O 2p orbitals contribute to the VBM, and Ti 3d orbitals contribute to the CBm with a wide band gap of 3.28 eV. The DOS of pristine $SrTiO_3$ is symmetric w.r.t. spin alignments (i.e., spin up or down), whereas in the case of N_O, the DOS is asymmetrical due to a devoid of an electron in comparison to pristine $SrTiO_3$ (see Figure 2a and 2b). In the latter case, some occupied states appeared above the pristine VBM, and some unoccupied discrete states can also be seen deep inside the forbidden region (since the N 2p orbitals have higher energy than the O 2p orbitals) (see Figure 2b). This leads to a reduction in the band gap. However, these midgap states increase the recombination rate and decrease the charge mobility which lead to degradation in the photocatalytic activity.

We have considered two sites for the substitution of Mn, viz., Sr and Ti sites. In the case of monodoping of Mn at the Sr site, the band gap (3.25 eV) is not getting reduced and thus cannot induce visible-light absorption (see Figure 2c). The occupied and unoccupied states of Mn orbitals appeared deep inside the valence and conduction band, respectively, indicating that Mn_{Sr} is very stable. However, in the case of Ti site substitution, we get interesting features in the DOS (see Figure 2d). The localized states bring down the CBm. Hence, the band gap is reduced to 2.57 eV, resulting in the visible-light absorption. However, due to a shift of the CBm in downward direction, its reduction power is degraded. Therefore, it can not be a potential candidate for H_2 production from water splitting.

In the case of codoping, the substitution of Mn at both sites, Sr and Ti in addition to N_O, helps to passivate the localized mid gap states (introduced by N substitution) and form continuum states as shown in Figure 2e and 2f. The passivation

https://dx.doi.org/10.1021/acs.jpcc.9b11160
J. Phys. Chem. C 2020, 124, 10272−10279

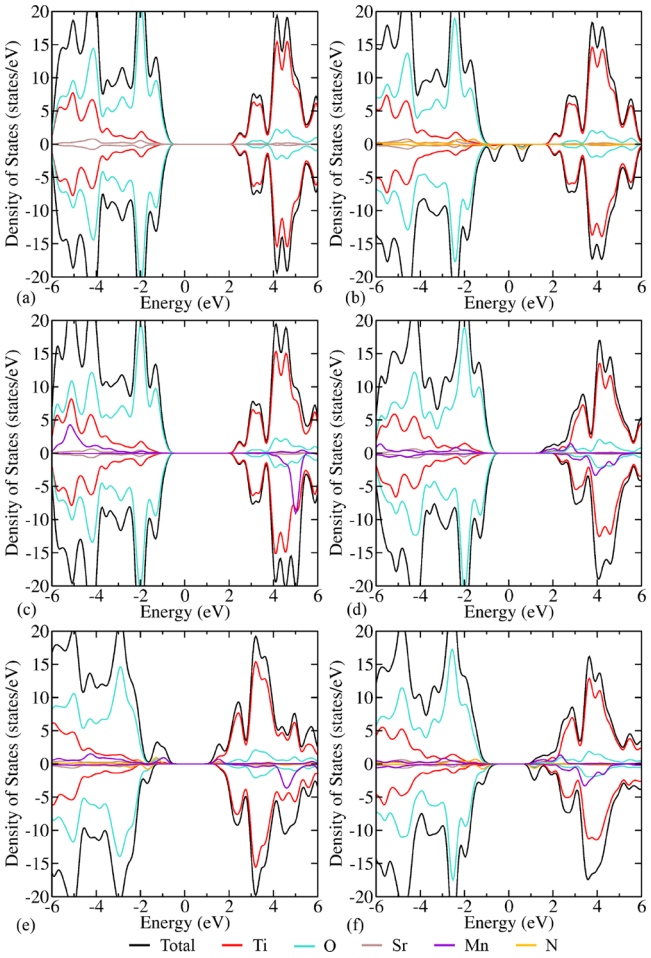

Figure 2. Electronic density of states for the supercell of (a) pristine $SrTiO_3$, (b) N_O, (c) Mn_{Sr}, (d) Mn_{Ti}, (e) $Mn_{Sr}N_O$, and (f) $Mn_{Ti}N_O$ type defects.

of states is concomitant with the hybridization of O and N orbitals and Mn and O orbitals in the $Mn_{Sr}N_O$ defect configuration as shown in Figure 2e (near the VBM). However, in the case of $Mn_{Ti}N_O$, Mn states arise only near the CBm as shown in Figure 2f. The recombination of photogenerated charge carriers is suppressed, and the diffusion and mobility are increased owing to the passivation of discrete localized states. The band gaps of $Mn_{Sr}N_O$ and $Mn_{Ti}N_O$ are 2.34 and 1.94 eV, respectively, which are the desirable ones for visible-light absorption. In the case of $Mn_{Ti}N_O$, CBm is shifted downward by a large amount and hence adversely affects the reduction power for hydrogen generation. However, in the case of $Mn_{Sr}N_O$, this downward shift is very small. Consequently, the codoping of Mn at the Sr site and N at the O site is favorable for overall photocatalytic water splitting. Also, from Figure 1c, we can see a relatively large distortion in the case of $Mn_{Sr}N_O$ codoping, which builds up the internal field, that is helpful for photogenerated charge carrier separation and thus enhances the photocatalytic efficiency. Therefore, $Mn_{Sr}N_O$ codoping in $SrTiO_3$ is a promising candidate to enhance the photocatalytic efficiency and generate hydrogen from water splitting.

Optical Properties. To determine the optical spectra, we have computed the frequency-dependent complex dielectric function $\epsilon(\omega) = \epsilon_1(\omega) + i\epsilon_2(\omega)$ using the G_0W_0@HSE06 approach (the results with HSE06 are shown in Figures S5 and S6). The real (ϵ_1) and imaginary (ϵ_2) parts of the dielectric function have been shown in Figure 3a and 3b, respectively.

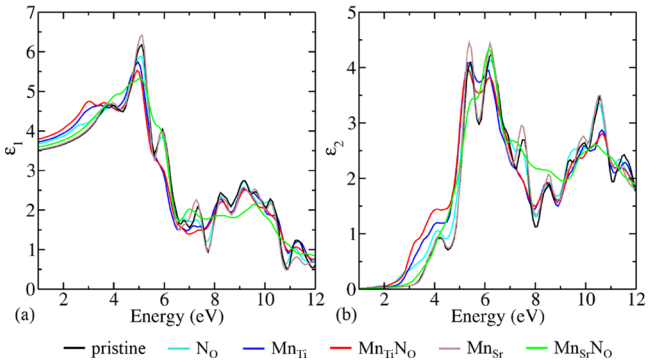

Figure 3. Spatially average (a) real (ϵ_1) and (b) imaginary (ϵ_2) part of the dielectric function obtained by G_0W_0@HSE06 for the pristine, monodoped, and codoped $SrTiO_3$.

The static ($\omega = 0$) real part of $\epsilon(\omega)$ for pristine $SrTiO_3$ is found to be 3.46, which is well in agreement with previous findings.[62] On doping, its value is increased (see Figure 3a). The imaginary part of the dielectric function represents the optical absorption (see Figure 3b). We have found the first peak at 4.20 eV for pristine $SrTiO_3$ [experimental value is 4.7 eV].[63] Note that the peaks are shifted toward the lower-energy region, except for Mn_{Sr}. Even if the exact numbers may differ from the experimental values, at least from the trends it is clear that the band gap is getting reduced on doping in $SrTiO_3$. Also, we could note that the onset of the absorption edge shifts toward the lower region. Hence, the optical response is shifted toward the visible region. The spectrum of Mn_{Sr} coincides with the pristine supercell of $SrTiO_3$ because there is no reduction in band gap, while in rest of the cases, band gap is reduced (see Figure 3b).

Band-Edge Alignment. Note that only a reduction in band gap can not ensure the hydrogen generation via photocatalytic water splitting. The band edges (VBM and CBm) should have appropriate position. For water splitting, the CBm must lie above the water reduction potential level (H^+/H_2), and the VBM must be positioned below the water oxidation potential level (O_2/H_2O). First, we have aligned the band edges of undoped $SrTiO_3$ w.r.t. water redox potential levels. The CBm lies 0.8 eV above the water reduction potential (H^+/H_2), and the VBM lies 1.25 eV below the water oxidation potential.[64] We see that the position of the CBm and VBM of the pristine $SrTiO_3$ is consistent with previous findings.[41] Thereafter, we align the band edges of doped $SrTiO_3$ by observing the shift in energy of the VBM and CBm w.r.t. undoped $SrTiO_3$. From Figure 4, we have found that in the case of N_O the VBM is shifted upward, and the CBm is not disturbed. However, some localized states are present deep in the forbidden region, which degrade the photocatalytic efficiency. Hence, N_O is not the promising one for water splitting. In the case of Mn_{Ti} and $Mn_{Ti}N_O$, the CBm is shifted downward by a large amount, and hence, their reduction power is very low and could not be utilized for hydrogen generation from water. On substituting Mn at the Sr site, the band gap is not getting reduced and thus not inducing the visible-light response. In the case of $Mn_{Sr}N_O$, CBm is shifted by a small amount and thus retains the reduction power. It has a desirable band gap of 2.34 eV and also does not contain any

https://dx.doi.org/10.1021/acs.jpcc.9b11160
J. Phys. Chem. C 2020, 124, 10272−10279

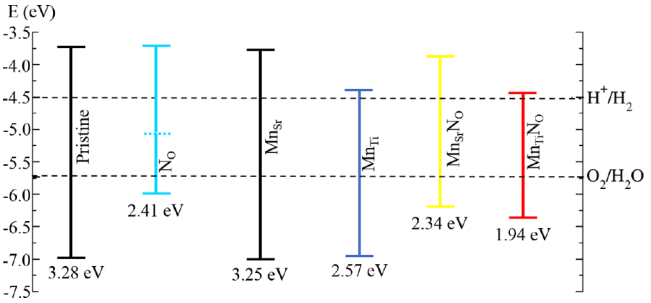

Figure 4. Band-edge alignment of (un)doped $SrTiO_3$ w.r.t. water redox potential levels (H^+/H_2, O_2/H_2O).

localized midgap states. In view of this, from the applicability in photocatalytic water splitting, only $Mn_{Sr}N_O$ is the most desirable one. Hence, these theoretical studies help in further future investigations to engineer a device that will be environmentally friendly.

Effective Mass for Pristine and $Mn_{Sr}N_O$-Codoped $SrTiO_3$. We have also determined the effective mass of electrons and holes for the pristine and $Mn_{Sr}N_O$-codoped $SrTiO_3$ configurations using the HSE06 functional (see Table 1). These have been obtained from the curvature of band edges by calculating the inverse of the second derivative of band energies with respect to k at the band edges. These values of effective masses for the pristine system (except for heavy hole) are validated by previous studies.[65−67]

Table 1. Effective Masses (In Terms of Free-Electron Mass m_e) at the Band Edge for Pristine and $Mn_{Sr}N_O$-Codoped $SrTiO_3$[a]

configuration	m_{he}	m_{le}	m_{hh}	m_{lh}
pristine	5.18	0.38	−10.36	−0.74
$Mn_{Sr}N_O$	5.09		−2.58	

[a]The masses m_{he}, m_{le}, m_{hh}, and m_{lh} correspond to heavy-electron, light-electron, heavy-hole, and light-hole bands, respectively.

We have used a supercell so that the periodic images of the defects do not interact and the defects get localized in the system. However, as the size of the supercell increases, the bands in the first (primitive) Brillouin zone of the primitive/normal cell get folded, and the supercell Brillouin zone shrinks. Consequently, the energy levels in the band structure become very dense, and thus, for a large supercell, we do not get much information from a band structure. Therefore, unfolding of the band structure is used in general to get a real picture of the band structure (for details, see refs 68 and 69). Despite the use of a supercell (which is not too big in our case), we can see from Figure 5 that the density of the bands near the VBM and CBm is not very high. Also, there is no overlap of bands at the VBM and CBm in codoped $SrTiO_3$. Therefore, band folding does not create much of a problem for these cases, and in principle, we can get the correct result for the effective masses.

From Figure 5a, we can see that the pristine has 3-fold degeneracy at the CBm (at the Γ k-point). This degeneracy is lifted as one moves away from the Γ k-point in the direction of the X, M, or R k-point. The effective mass of electron/hole due to a heavy-, light-electron/hole, and spin split-off band is obtained along the high-symmetry Γ−X path for pristine $SrTiO_3$. The effective mass of the electron/hole corresponding to a spin split-off band is found to be the same as that for the light-electron/hole band.

After the validation for the pristine system, we have calculated the effective mass for $Mn_{Sr}N_O$. From Figure 5b, we can see that there is no degeneracy of the band at CBm and VBM. The defect states constitute the CBm and VBM, which are contributed by the codoping of Mn at the Sr site and N at the O site. The flat bands (smaller curvature) indicate that the defect is localized in the system. The CBm for $Mn_{Sr}N_O$ lies at the [0.2 0.2 0.2] k-point, and the VBM lies at the R k-point. The effective mass of the electron is $5.09m_e$ and $3.04m_e$ along [0.2 0.2 0.2]-Γ and [0.2 0.2 0.2]-X directions, respectively. This implies the anisotropy in effective mass. The effective mass of the hole is $-2.58m_e$ and $-1.53m_e$ along the R−Γ and R−X directions, respectively. The comparable values of effective mass of electrons for codoped and pristine systems indicate that the mobility will not be affected much due to the shallower defect level. Note that the mobility depends on the effective mass as well as on scattering (relaxation) time. The scattering rate will decrease on doping as the degeneracy is lifted, and thus despite a small increment in effective mass, the mobility will not be affected much, especially here as the doping concentration is very low. These effective mass studies further assist future experimental and theoretical investigations to tailor the transport properties of the system.

CONCLUSIONS

In summary, we have systematically studied the thermodynamic stability of different types of dopants and codopants in $SrTiO_3$ using hybrid DFT and *ab initio* thermodynamics. Our

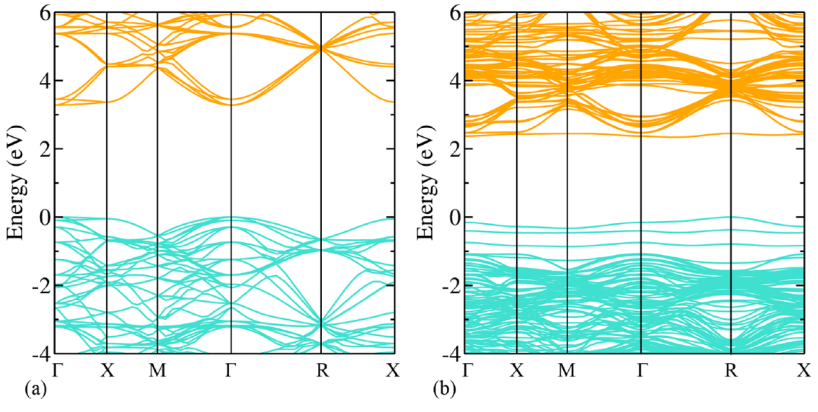

Figure 5. Band structure calculated using the hybrid (HSE06) functional of (a) pristine $SrTiO_3$ and (b) $Mn_{Sr}N_O$-codoped $SrTiO_3$.

https://dx.doi.org/10.1021/acs.jpcc.9b11160
J. Phys. Chem. C 2020, 124, 10272−10279

results indicate that $Mn_{Sr}N_O$ is the stable defect configuration under equilibrium growth conditions. We have found that despite monodopant-related defects help in reducing the band gap they generate localized states deep inside the band gap. These states act as recombination centers, which in turn reduce the photocatalytic efficiency. Thus, monodoping of both N or Mn can induce visible-light absorption, but none of them are suitable for photocatalytic activity. The codoping reduces the band gap to the ideal visible region as well as passivates the localized states to form the continuous band with suitable band-edge positions. We have observed that the calculated effective mass of electrons for the codoped system is found to be similar to that of the pristine system. This indicates that electron mobility is not reduced much due to the shallower defect level. We find that $Mn_{Sr}N_O$-codoped $SrTiO_3$ could be a potential candidate for producing hydrogen via photocatalytic water splitting.

■ ASSOCIATED CONTENT

Supporting Information

The Supporting Information is available free of charge at https://pubs.acs.org/doi/10.1021/acs.jpcc.9b11160.

Details of choice of the codopants and chemical potentials, validation of exchange-correlation functional, and optical response using hybrid functional (PDF)

■ AUTHOR INFORMATION

Corresponding Authors

Manish Kumar − *Department of Physics, Indian Institute of Technology Delhi, New Delhi, India*; Email: manish.kumar@physics.iitd.ac.in

Saswata Bhattacharya − *Department of Physics, Indian Institute of Technology Delhi, New Delhi, India*; orcid.org/0000-0002-4145-4899; Phone: +91-11-2659 1359; Email: saswata@physics.iitd.ac.in; Fax: +91-11-2658 2037

Authors

Pooja Basera − *Department of Physics, Indian Institute of Technology Delhi, New Delhi, India*

Shikha Saini − *Department of Physics, Indian Institute of Technology Delhi, New Delhi, India*

Complete contact information is available at: https://pubs.acs.org/10.1021/acs.jpcc.9b11160

Notes

The authors declare no competing financial interest.

■ ACKNOWLEDGMENTS

M.K. acknowledges CSIR, India, for the junior research fellowship [grant no. 09/086(1292)/2017-EMR-I]. P.B. acknowledges UGC, India, for the senior research fellowship [grant no. 20/12/2015 (ii) EU-V]. S.S. acknowledges CSIR, India, for the senior research fellowship [grant no. 09/086 (1231)/2015-EMR-I]. S.B. acknowledges the financial support from SERB under a core research grant (grant no. CRG/2019/000647). We acknowledge the High Performance Computing (HPC) facility at IIT Delhi for computational resources.

■ REFERENCES

(1) Chen, X.; Shen, S.; Guo, L.; Mao, S. S. Semiconductor-based photocatalytic hydrogen generation. *Chem. Rev.* **2010**, *110*, 6503−6570.

(2) Chen, C.; Ma, W.; Zhao, J. Semiconductor-mediated photodegradation of pollutants under visible-light irradiation. *Chem. Soc. Rev.* **2010**, *39*, 4206−4219.

(3) Kudo, A.; Miseki, Y. Heterogeneous photocatalyst materials for water splitting. *Chem. Soc. Rev.* **2009**, *38*, 253−278.

(4) Kubacka, A.; Fernández-García, M.; Colón, G. Advanced nanoarchitectures for solar photocatalytic applications. *Chem. Rev.* **2012**, *112*, 1555−1614.

(5) Bhattacharya, S.; Xiong, Z.; Wu, G.; Chen, P.; Feng, Y. P.; Majumder, C.; Das, G. P. Dehydrogenation Mechanism of Monoammoniated Lithium Amidoborane $[Li(NH_3)NH_2BH_3]$. *J. Phys. Chem. C* **2012**, *116* (16), 8859−8864.

(6) Bhattacharya, S.; Wu, G.; Ping, C.; Feng, Y. P.; Das, G. P. Lithium Calcium Imide $[Li_2Ca(NH)_2]$ for Hydrogen Storage: Structural and Thermodynamic Properties. *J. Phys. Chem. B* **2008**, *112*, 11381−11384.

(7) Manikandan, M.; Tanabe, T.; Li, P.; Ueda, S.; Ramesh, G. V.; Kodiyath, R.; Wang, J.; Hara, T.; Dakshanamoorthy, A.; Ishihara, S.; et al. Photocatalytic water splitting under visible light by mixed-valence Sn_3O_4. *ACS Appl. Mater. Interfaces* **2014**, *6*, 3790−3793.

(8) Zhao, P.; Liang, Y.; Ma, Y.; Huang, B.; Dai, Y. Janus chromium dichalcogenide monolayers with low carrier recombination for photocatalytic overall water-splitting under infrared light. *J. Phys. Chem. C* **2019**, *123*, 4186−4192.

(9) Domen, K.; Kudo, A.; Onishi, T.; Kosugi, N.; Kuroda, H. Photocatalytic decomposition of water into hydrogen and oxygen over nickel(II) oxide-strontium titanate ($SrTiO_3$) powder. 1. Structure of the catalysts. *J. Phys. Chem.* **1986**, *90*, 292−295.

(10) Ahuja, S.; Kutty, T. Nanoparticles of $SrTiO_3$ prepared by gel to crystallite conversion and their photocatalytic activity in the mineralization of phenol. *J. Photochem. Photobiol., A* **1996**, *97*, 99−107.

(11) Iwashina, K.; Kudo, A. Rh-doped $SrTiO_3$ photocatalyst electrode showing cathodic photocurrent for water splitting under visible-light irradiation. *J. Am. Chem. Soc.* **2011**, *133*, 13272−13275.

(12) Zhang, Q.; Huang, Y.; Xu, L.; Cao, J.-j.; Ho, W.; Lee, S. C. Visible-light-active plasmonic Ag-$SrTiO_3$ nanocomposites for the degradation of NO in air with high selectivity. *ACS Appl. Mater. Interfaces* **2016**, *8*, 4165−4174.

(13) Niishiro, R.; Tanaka, S.; Kudo, A. Hydrothermal-synthesized $SrTiO_3$ photocatalyst codoped with rhodium and antimony with visible-light response for sacrificial H_2 and O_2 evolution and application to overall water splitting. *Appl. Catal., B* **2014**, *150−151*, 187−196.

(14) Tan, H.; Zhao, Z.; Zhu, W.-b.; Coker, E. N.; Li, B.; Zheng, M.; Yu, W.; Fan, H.; Sun, Z. Oxygen vacancy enhanced photocatalytic activity of pervoskite $SrTiO_3$. *ACS Appl. Mater. Interfaces* **2014**, *6*, 19184−19190.

(15) Zhang, K. H. L.; Wu, R.; Tang, F.; Li, W.; Oropeza, F. E.; Qiao, L.; Lazarov, V. K.; Du, Y.; Payne, D. J.; MacManus-Driscoll, J. L.; et al. Electronic structure and band alignment at the NiO and $SrTiO_3$ p-n heterojunctions. *ACS Appl. Mater. Interfaces* **2017**, *9*, 26549−26555.

(16) Konta, R.; Ishii, T.; Kato, H.; Kudo, A. Photocatalytic activities of noble metal ion doped $SrTiO_3$ under visible light irradiation. *J. Phys. Chem. B* **2004**, *108*, 8992−8995.

(17) Chen, H.-C.; Huang, C.-W.; Wu, J. C. S.; Lin, S.-T. Theoretical investigation of the metal-doped $SrTiO_3$ photocatalysts for water splitting. *J. Phys. Chem. C* **2012**, *116*, 7897−7903.

(18) Niishiro, R.; Kato, H.; Kudo, A. Nickel and either tantalum or niobium-codoped TiO_2 and $SrTiO_3$ photocatalysts with visible-light response for H_2 or O_2 evolution from aqueous solutions. *Phys. Chem. Chem. Phys.* **2005**, *7*, 2241−2245.

(19) Yu, H.; Ouyang, S.; Yan, S.; Li, Z.; Yu, T.; Zou, Z. Solgel hydrothermal synthesis of visible-light-driven Cr-doped $SrTiO_3$ for efficient hydrogen production. *J. Mater. Chem.* **2011**, *21*, 11347−11351.

(20) Kawasaki, S.; Nakatsuji, K.; Yoshinobu, J.; Komori, F.; Takahashi, R.; Lippmaa, M.; Mase, K.; Kudo, A. Epitaxial Rh-doped

$SrTiO_3$ thin film photocathode for water splitting under visible light irradiation. *Appl. Phys. Lett.* **2012**, *101*, 033910.
(21) Liu, P.; Nisar, J.; Pathak, B.; Ahuja, R. Hybrid density functional study on $SrTiO_3$ for visible light photocatalysis. *Int. J. Hydrogen Energy* **2012**, *37*, 11611−11617.
(22) Guo, Y.; Qiu, X.; Dong, H.; Zhou, X. Trends in non-metal doping of the $SrTiO_3$ surface: A hybrid density functional study. *Phys. Chem. Chem. Phys.* **2015**, *17*, 21611−21621.
(23) Wang, J.; Yin, S.; Komatsu, M.; Zhang, Q.; Saito, F.; Sato, T. Preparation and characterization of nitrogen doped $SrTiO_3$ photocatalyst. *J. Photochem. Photobiol., A* **2004**, *165*, 149−156.
(24) Mi, Y. Y.; Wang, S. J.; Chai, J. W.; Pan, J. S.; Huan, C. H. A.; Feng, Y. P.; Ong, C. K. Effect of nitrogen doping on optical properties and electronic structures of $SrTiO_3$ films. *Appl. Phys. Lett.* **2006**, *89*, 231922.
(25) Zhang, C.; Jia, Y.; Jing, Y.; Yao, Y.; Ma, J.; Sun, J. Effect of non-metal elements (B, C, N, F, P, S) mono-doping as anions on electronic structure of $SrTiO_3$. *Comput. Mater. Sci.* **2013**, *79*, 69−74.
(26) Zou, F.; Jiang, Z.; Qin, X.; Zhao, Y.; Jiang, L.; Zhi, J.; Xiao, T.; Edwards, P. P. Template-free synthesis of mesoporous N-doped $SrTiO_3$ perovskite with high visible-light-driven photocatalytic activity. *Chem. Commun.* **2012**, *48*, 8514−8516.
(27) Reunchan, P.; Ouyang, S.; Umezawa, N.; Xu, H.; Zhang, Y.; Ye, J. Theoretical design of highly active $SrTiO_3$-based photocatalysts by a codoping scheme towards solar energy utilization for hydrogen production. *J. Mater. Chem. A* **2013**, *1*, 4221−4227.
(28) Ouyang, S.; Tong, H.; Umezawa, N.; Cao, J.; Li, P.; Bi, Y.; Zhang, Y.; Ye, J. Surface-alkalinization-induced enhancement of photocatalytic H_2 evolution over $SrTiO_3$-based photocatalysts. *J. Am. Chem. Soc.* **2012**, *134*, 1974−1977.
(29) Comes, R. B.; Sushko, P. V.; Heald, S. M.; Colby, R. J.; Bowden, M. E.; Chambers, S. A. Band-gap reduction and dopant interaction in epitaxial La,Cr co-doped $SrTiO_3$ thin films. *Chem. Mater.* **2014**, *26*, 7073−7082.
(30) Miyauchi, M.; Takashio, M.; Tobimatsu, H. Photocatalytic activity of $SrTiO_3$ codoped with nitrogen and lanthanum under visible light illumination. *Langmuir* **2004**, *20*, 232−236.
(31) Chen, W.; Liu, H.; Li, X.; Liu, S.; Gao, L.; Mao, L.; Fan, Z.; Shangguan, W.; Fang, W.; Liu, Y. Polymerizable complex synthesis of $SrTiO_3$: (Cr/Ta) photocatalysts to improve photocatalytic water splitting activity under visible light. *Appl. Catal., B* **2016**, *192*, 145−151.
(32) Gai, Y.; Li, J.; Li, S.-S.; Xia, J.-B.; Wei, S.-H. Design of narrow-gap TiO_2: A passivated codoping approach for enhanced photoelectrochemical activity. *Phys. Rev. Lett.* **2009**, *102*, 036402.
(33) Wei, W.; Dai, Y.; Guo, M.; Yu, L.; Huang, B. Density functional characterization of the electronic structure and optical properties of N-Doped, La-Doped, and N/La-codoped $SrTiO_3$. *J. Phys. Chem. C* **2009**, *113*, 15046−15050.
(34) Wei, W.; Dai, Y.; Guo, M.; Yu, L.; Jin, H.; Han, S.; Huang, B. Codoping synergistic effects in N-doped $SrTiO_3$ for higher energy conversion efficiency. *Phys. Chem. Chem. Phys.* **2010**, *12*, 7612−7619.
(35) Modak, B.; Ghosh, S. K. Role of F in improving the photocatalytic activity of Rh-doped $SrTiO_3$. *J. Phys. Chem. C* **2015**, *119*, 7215−7224.
(36) Zhu, W.; Qiu, X.; Iancu, V.; Chen, X.-Q.; Pan, H.; Wang, W.; Dimitrijevic, N. M.; Rajh, T.; Meyer, H. M.; Paranthaman, M. P.; et al. Band gap narrowing of titanium oxide semiconductors by noncompensated anion-cation codoping for enhanced visible-light photoactivity. *Phys. Rev. Lett.* **2009**, *103*, 226401.
(37) Parks Cheney, C.; Vilmercati, P.; Martin, E. W.; Chiodi, M.; Gavioli, L.; Regmi, M.; Eres, G.; Callcott, T. A.; Weitering, H. H.; Mannella, N. Origins of electronic band gap reduction in Cr/N codoped TiO_2. *Phys. Rev. Lett.* **2014**, *112*, 036404.
(38) Modak, B.; Ghosh, S. K. Enhancement of visible light photocatalytic activity of $SrTiO_3$: A hybrid density functional study. *J. Phys. Chem. C* **2015**, *119*, 23503−23514.
(39) Le Bahers, T.; Takanabe, K. Combined theoretical and experimental characterizations of semiconductors for photoelectrocatalytic applications. *J. Photochem. Photobiol., C* **2019**, *40*, 212−233.
(40) Walter, M. G.; Warren, E. L.; McKone, J. R.; Boettcher, S. W.; Mi, Q.; Santori, E. A.; Lewis, N. S. Solar water splitting cells. *Chem. Rev.* **2010**, *110*, 6446−6473.
(41) Stevanović, V.; Lany, S.; Ginley, D. S.; Tumas, W.; Zunger, A. Assessing capability of semiconductors to split water using ionization potentials and electron affinities only. *Phys. Chem. Chem. Phys.* **2014**, *16*, 3706−3714.
(42) Sun, T.; Lu, M. Modification of $SrTiO_3$ surface by nitrogen ion bombardment for enhanced photocatalysis. *Appl. Surf. Sci.* **2013**, *274*, 176−180.
(43) Liu, C. M.; Zu, X. T.; Zhou, W. L. Photoluminescence of nitrogen doped $SrTiO_3$. *J. Phys. D: Appl. Phys.* **2007**, *40*, 7318−7322.
(44) Tkach, A.; Vilarinho, P. M.; Kholkin, A. L. Structure-microstructure-dielectric tunability relationship in Mn-doped strontium titanate ceramics. *Acta Mater.* **2005**, *53*, 5061−5069.
(45) Yang, H.; Kotula, P. G.; Sato, Y.; Chi, M.; Ikuhara, Y.; Browning, N. D. Segregation of Mn^{2+} dopants as interstitials in $SrTiO_3$ grain boundaries. *Mater. Res. Lett.* **2014**, *2*, 16−22.
(46) Hohenberg, P.; Kohn, W. Inhomogeneous electron gas. *Phys. Rev.* **1964**, *136*, B864−B871.
(47) Kohn, W.; Sham, L. J. Self-consistent equations including exchange and correlation effects. *Phys. Rev.* **1965**, *140*, A1133−A1138.
(48) Bhattacharya, S.; Berger, D.; Reuter, K.; Ghiringhelli, L. M.; Levchenko, S. V. Theoretical evidence for unexpected O-rich phases at corners of MgO surfaces. *Phys. Rev. Materials* **2017**, *1*, 071601.
(49) Hedin, L. New method for calculating the one-particle Green's function with application to the electron-gas problem. *Phys. Rev.* **1965**, *139*, A796−A823.
(50) Hybertsen, M. S.; Louie, S. G. First-principles theory of quasiparticles: Calculation of band gaps in semiconductors and insulators. *Phys. Rev. Lett.* **1985**, *55*, 1418−1421.
(51) Kresse, G.; Furthmüller, J. Efficiency of ab-initio total energy calculations for metals and semiconductors using a plane-wave basis set. *Comput. Mater. Sci.* **1996**, *6*, 15−50.
(52) Kresse, G.; Joubert, D. From ultrasoft pseudopotentials to the projector augmented-wave method. *Phys. Rev. B: Condens. Matter Mater. Phys.* **1999**, *59*, 1758−1775.
(53) Blöchl, P. E. Projector augmented-wave method. *Phys. Rev. B: Condens. Matter Mater. Phys.* **1994**, *50*, 17953.
(54) Krukau, A. V.; Vydrov, O. A.; Izmaylov, A. F.; Scuseria, G. E. Influence of the exchange screening parameter on the performance of screened hybrid functionals. *J. Chem. Phys.* **2006**, *125*, 224106.
(55) Monkhorst, H. J.; Pack, J. D. Special points for Brillouin-zone integrations. *Phys. Rev. B* **1976**, *13*, 5188−5192.
(56) Basera, P.; Saini, S.; Arora, E.; Singh, A.; Kumar, M.; Bhattacharya, S. Stability of non-metal dopants to tune the photoabsorption of TiO_2 at realistic temperatures and oxygen partial pressures: A hybrid DFT study. *Sci. Rep.* **2019**, *9*, 1−13.
(57) Bhattacharya, A.; Bhattacharya, S. Unraveling the role of vacancies in the potentially promising thermoelectric clathrates $Ba_8Zn_xGe_{46-x-y}\square_y$. *Phys. Rev. B: Condens. Matter Mater. Phys.* **2016**, *94*, 094305.
(58) Bhattacharya, S.; Levchenko, S. V.; Ghiringhelli, L. M.; Scheffler, M. Efficient ab initio schemes for finding thermodynamically stable and metastable atomic structures: Benchmark of cascade genetic algorithms. *New J. Phys.* **2014**, *16*, 123016.
(59) Bhattacharya, A.; Bhattacharya, S. Exploring N-rich phases in Li_xN_y clusters for hydrogen storage at nanoscale. *J. Phys. Chem. Lett.* **2015**, *6*, 3726−3730.
(60) Arora, E.; Saini, S.; Basera, P.; Kumar, M.; Singh, A.; Bhattacharya, S. Elucidating the role of temperature and pressure to the thermodynamic stability of charged defects in complex metal-hydrides: A case study of $NaAlH_4$. *J. Phys. Chem. C* **2019**, *123*, 62−69.
(61) Li, J.; Wei, S.-H.; Li, S.-S.; Xia, J.-B. Design of shallow acceptors in ZnO: First-principles band-structure calculations. *Phys. Rev. B: Condens. Matter Mater. Phys.* **2006**, *74*, 081201.

https://dx.doi.org/10.1021/acs.jpcc.9b11160
J. Phys. Chem. C 2020, 124, 10272−10279

(62) Ergönenc, Z.; Kim, B.; Liu, P.; Kresse, G.; Franchini, C. Converged *GW* quasiparticle energies for transition metal oxide perovskites. *Phys. Rev. Materials* **2018**, *2*, 024601.
(63) Cardona, M. Optical properties and band structure of $SrTiO_3$ and $BaTiO_3$. *Phys. Rev.* **1965**, *140*, A651−A655.
(64) Xu, Y.; Schoonen, M. A. A. The absolute energy positions of conduction and valence bands of selected semiconducting minerals. *Am. Mineral.* **2000**, *85*, 543−556.
(65) Janotti, A.; Steiauf, D.; Van de Walle, C. G. Strain effects on the electronic structure of $SrTiO_3$: Toward high electron mobilities. *Phys. Rev. B: Condens. Matter Mater. Phys.* **2011**, *84*, 201304.
(66) Marques, M.; Teles, L. K.; Anjos, V.; Scolfaro, L. M. R.; Leite, J. R.; Freire, V. N.; Farias, G. A.; da Silva, E. F. Full-relativistic calculations of the $SrTiO_3$ carrier effective masses and complex dielectric function. *Appl. Phys. Lett.* **2003**, *82*, 3074−3076.
(67) Fadlallah, M. M.; Shibl, M. F.; Vlugt, T. J. H.; Schwingenschlogl, U. Theoretical study on cation codoped $SrTiO_3$ photocatalysts for water splitting. *J. Mater. Chem. A* **2018**, *6*, 24342−24349.
(68) Ku, W.; Berlijn, T.; Lee, C.-C. Unfolding first-principles band structures. *Phys. Rev. Lett.* **2010**, *104*, 216401.
(69) Popescu, V.; Zunger, A. Extracting *E* versus $\vec{k}$ effective band structure from supercell calculations on alloys and impurities. *Phys. Rev. B: Condens. Matter Mater. Phys.* **2012**, *85*, 085201.

https://dx.doi.org/10.1021/acs.jpcc.9b11160
J. Phys. Chem. C 2020, 124, 10272−10279